Scientific Reports

https://doi.org/10.1038/s41598-026-47270-7

Article in Press

Multi-timescale energy-aware grid-forming control with self-tuning virtual inductance for battery lifetime enhancement

Received: 29 September 2025

Accepted: 31 March 2026

Published online: 03 April 2026

Cite this article as: Zheng L. & Liu X. Multi-timescale energy-aware grid-forming control with self-tuning virtual inductance for battery lifetime enhancement. *Sci Rep* (2026). https://doi.org/10.1038/s41598-026-47270-7

Lijun Zheng & Xinghu Liu

Multi-Timescale Energy-Aware Grid-Forming Control with Self-Tuning Virtual Inductance for Battery Lifetime Enhancement

Lijun Zheng[1,*], Weijie Chen[2]

[1] Zhijiang college of zhejiang university of technology, Shaoxing, China; zhenglijun@zzjc.edu.cn

[2]Zhejiang University of Technology, Hangzhou, Zhejiang, 310014, China

zhenglijun@zzjc.edu.cn; wjcper2008@163.com

* Correspondence: zhenglijun@zzjc.edu.cn

Abstract: With the increasing penetration of converter-interfaced renewable energy, modern power systems are increasingly exposed to weak-grid conditions, where reduced short-circuit strength and low inertia significantly challenge the stability of grid-forming inverters. To address these issues, this paper proposes a multi-timescale energy-aware grid-forming (GFM) control strategy for PV–battery energy storage systems (PV–BES). The fast layer provides immediate stabilization by shaping the inverter output impedance and injecting virtual damping. The medium layer adaptively tunes the virtual inertia and damping gains according to the estimated DC-link energy and the online-evaluated grid strength, enabling the inverter to autonomously regulate its dynamic behavior under varying operating conditions. A slow layer regulates long-term energy trajectories to reduce battery cycling stress. In addition, a dedicated mode coordinator is introduced to ensure smooth transitions among MPPT, charging/discharging, and GFM operation, preventing discontinuities in DC-link energy and adaptive control gains. Numerical simulations demonstrate that the proposed strategy effectively enhances transient stability, suppresses oscillatory responses under weak-grid disturbances, and significantly mitigates battery degradation by reducing DC-link energy fluctuations. These results highlight the potential of incorporating energy-awareness into GFM control design for achieving both improved dynamic performance and extended battery lifetime.

Keywords: Multi-timescale control, energy-aware grid-forming, BES system, self-tuning virtual inductance, battery lifetime extension, weak grid stability.

1. Introduction

The accelerating integration of renewable energy sources (RES) into power systems has become a defining characteristic of the global energy transition [1], [2]. Among the various RES technologies, photovoltaic (PV) generation has emerged as a dominant contributor due to its modularity, rapidly declining costs, and environmental benefits [1]-[3]. According to recent reports, the global installed capacity of PV has surpassed hundreds of gigawatts, and it is projected to continue growing as nations pursue carbon neutrality targets and sustainable development goals [2], [4]. Simultaneously, battery energy storage systems (BESs) are gaining traction as complementary assets that mitigate the variability and intermittency of PV generation, providing both short-term power balancing and long-term energy management [5]-[7]. The synergy between PV generation and BES enables enhanced flexibility, improves the utilization of renewable energy, and contributes to grid resilience in the face of disturbances [6], [7].

Despite these advantages, the increasing penetration of inverter-based resources (IBRs) poses significant challenges to the stability and reliability of modern power systems [8], [9]. Traditional synchronous generators inherently provide inertia and damping due to their rotating masses, stabilizing frequency and voltage fluctuations [3]. In contrast, IBRs interface through power electronic converters and inherently lack physical inertia, reducing the system’s ability to withstand disturbances [8]–[10]. The decline in system strength is particularly problematic in weak grids, where low short-circuit ratios amplify the impact of disturbances and create difficulties for synchronization and fault ride-through capabilities [9], [10].

To address these challenges, researchers have proposed a wide range of grid-forming (GFM) control strategies. Classical methods include droop control, which emulates the frequency–power and voltage–reactive power characteristics of synchronous machines, thereby enabling autonomous sharing of active and reactive power among parallel inverters [11], [12]. Variants such as virtual synchronous machine (VSM) and virtual oscillator control (VOC) further enhance transient stability by embedding virtual inertia and damping into the control loops [13]–[15]. These methods allow grid-forming inverters to provide grid support services like frequency regulation, voltage control, and black-start capability. However, most implementations rely on fixed parameter settings [11], [13]. In practice, the grid operating condition is highly dynamic, with varying levels of renewable generation, load demand, and network

impedance. Fixed-parameter controllers struggle to maintain optimal performance across this wide range of conditions [12], [16].

Another critical limitation of existing GFM strategies lies in their limited consideration of energy storage aging. Batteries are key enablers of PV integration, but their operational lifetime is sensitive to state-of-charge (SOC) swings, depth of discharge (DoD), and high-frequency current ripples introduced by converter dynamics. Studies have shown that frequent charge–discharge cycling accelerates capacity fading and increases the internal resistance of batteries, leading to higher lifecycle costs and reduced reliability [17]–[19]. Conventional GFM methods primarily target system-level stability without explicitly accounting for the long-term health of BES assets. This mismatch creates a conflict between the immediate need for fast frequency/voltage support and the long-term objective of maximizing battery lifespan [12], [16]–[19].

Additionally, with the growing deployment of multiple units in microgrids and distribution feeders, the coordination challenge has become increasingly significant. Poorly coordinated inverters can lead to unequal power sharing, circulating currents, and potential control instability. While centralized approaches have been proposed, they suffer from communication delays, high costs, and lack of scalability. Decentralized strategies based on droop control or fixed virtual impedance often cannot adequately adapt to diverse system dynamics or battery health states [11], [12], [16], [20].

To fully support stable operation under weak-grid conditions, the proposed multi-timescale framework incorporates a medium layer that adaptively adjusts the virtual inertia and damping according to the estimated DC-link energy and the online-evaluated grid strength. This layer bridges the fast stabilizing mechanisms and the slow energy-oriented supervisory control, enabling the inverter to autonomously reshape its dynamic characteristics when operating conditions vary. In addition, a mode coordination mechanism is introduced to guarantee seamless transitions among PV MPPT, battery charging/discharging, and grid-forming operation. Without such coordination, abrupt changes in operating mode may lead to discontinuities in DC-link energy trajectories and cause undesirable jumps in adaptive control gains. The embedded mode coordinator ensures smooth transitions and preserves the underlying assumptions of the energy-aware control strategy.

To bridge these gaps, this paper proposes a cross-timescale energy-aware grid-forming (CTEA-GFM) control strategy tailored for renewable energy storage system systems. The core idea is to decouple the control problem into two complementary layers: The main contributions of this paper can be summarized as follows:

1. Multi-timescale energy-aware GFM control: A hierarchical structure combining a fast DC-link energy-based virtual inductance regulation loop with a slow battery-life-oriented power sharing loop, ensuring both transient stability and long-term durability.

2. Self-tuning virtual inductance: A regulation law that dynamically adapts the virtual inductance according to DC-link voltage and grid-strength estimation, with bounded rate-limiting and filtering to avoid instability.

3. Battery-lifetime-friendly coordination: An energy-aware slow-layer and mode coordination mechanism that mitigates long-term battery stress by suppressing DC-link energy ripple and avoiding unnecessary charge–discharge cycling during operating mode transitions, without introducing an explicit state-of-charge or long-term energy management control loop.

The remainder of this paper is structured as follows. Section 2 presents the system configuration and basic control strategy of the system. Section 3 details the proposed multi-timescale energy-aware GFM control strategy. Stability analysis and battery lifetime modeling are presented in Section 4. Simulation results and performance analyses are discussed in Section 5. Finally, Section 6 provides concluding remarks.

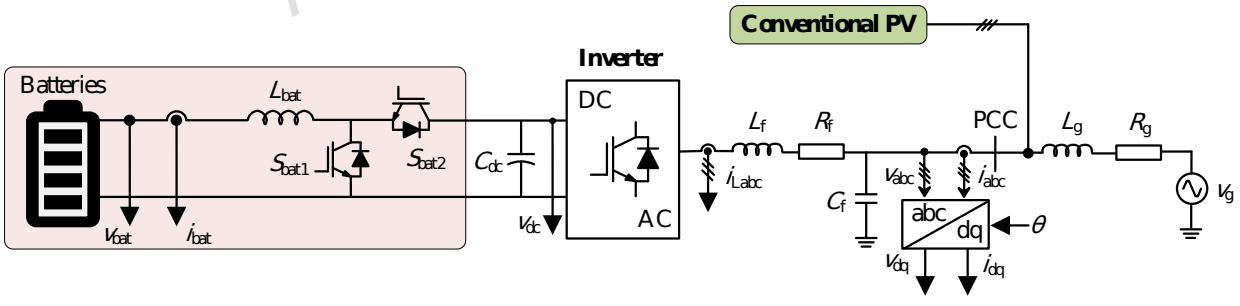

Figure 1. Configuration of the -BES system.

2. System Description and Basic Control

2.1. PV-BE System Description

The system, as shown in Fig. 1, consists of a battery energy storage system (BES), a bidirectional DC–DC converter, a DC/AC inverter with an LC filter, and the grid interface at the point of common coupling (PCC). In addition, a conventional PV source is connected in parallel to support the power supply. It is noted that the PV subsystem is connected through a dedicated DC/DC converter rather than directly interfacing with the DC-link. This architecture is widely adopted in hybrid PV–BESS systems because it decouples the fast GFM voltage-regulation dynamics from the irradiance-driven fluctuations of the PV array. Although the PV does not directly influence the DC-link voltage, its long-term energy contribution affects the battery operating trajectory and therefore plays a crucial role in the energy-aware GFM strategy. This justifies the relevance of the PV subsystem within the proposed framework. It should be clarified that the PV subsystem with maximum power point tracking (MPPT) is not introduced as a long-term energy management or state-of-charge regulation mechanism in this work. Instead, it is included to represent a realistic and structured source of power variability that directly interacts with the DC-link dynamics in practical PV–BES systems.

Unlike arbitrary disturbances injected at the PCC, the PV system operating under MPPT introduces physically constrained, time-correlated, and operating-condition-dependent power variations driven by changes in irradiance and temperature. These variations originate from the DC side and lead to sustained, non-periodic energy imbalance at the DC-link, which fundamentally differs from artificial step or impulse disturbances applied on the AC side.

The significance of the PV subsystem in this study lies in demonstrating that the proposed energy-aware grid-forming controller can effectively suppress DC-link energy ripple and maintain stable grid-forming operation under realistic renewable-driven conditions, without relying on higher-level energy scheduling or SoC-based control. The MPPT-controlled PV therefore provides a representative and practically relevant excitation scenario in which renewable power fluctuations simultaneously stress the DC-link, the battery, and the grid-forming control loop.

In contrast, disturbances applied at the PCC are mainly used to evaluate transient robustness and small-signal stability of the AC-side grid-forming behavior. Together, these two types of excitation illustrate that the proposed controller can handle both renewable-induced DC-side variability and externally imposed AC-side disturbances without compromising stability or performance.

A. Battery Energy Storage and DC–DC Converter

The BES system provides the DC voltage v_{bat} and current i_{bat}. A bidirectional half-bridge converter, composed of switches S_{bat1} and S_{bat2} and the series inductor L_{bat}, regulates the charging and discharging process of the battery. The governing dynamics can be expressed as:

$$L_{bat}\frac{di_{bat}}{dt} = v_{bat} - d_{bat}v_{dc}, \tag{1}$$

where d_{bat} is the duty ratio of the DC–DC converter and vdc denotes the DC-link voltage. The DC-link capacitor C_{dc} buffers the power mismatch between the DC source and the inverter:

$$C_{dc}\frac{dv_{dc}}{dt} = i_{bat} - i_{inv}, \tag{2}$$

where i_{inv} is the input current of the DC/AC inverter.

B. Inverter and LC Filter

The inverter bridges the DC and AC sides, converting the DC-link voltage into three-phase AC currents i_{Labc}. These currents flow through the LC filter consisting of L_f, and C_f. The filter dynamics are given by:

$$L_f\frac{di_{Labc}}{dt} = v_{inv} - v_{cf} - R_f i_{Labc}, \tag{3}$$

$$C_f\frac{dv_{cf}}{dt} = i_{Labc} - i_{abc}, \tag{4}$$

where v_{inv} is the inverter output voltage, v_{cf} is the capacitor voltage, and i_{abc} denotes the injected current into the PCC.

C. Grid Interface

At the PCC, the inverter currents are injected into the grid through the line impedance modeled by L_g and R_g. The grid dynamics can be expressed as:

$$L_g\frac{di_{abc}}{dt} = v_{cf} - v_g - R_g i_{abc}, \tag{5}$$

where v_g is the grid voltage. The grid angle θ is obtained from the active power control loop of the GFM control for synchronizing the inverter with the utility grid and enabling the transformation between the stationary *abc* frame and the synchronous *dq* frame.

D. PV Integration

A conventional PV source is connected at the PCC in parallel with the BES–inverter system. The PV operates under the MPPT scheme and directly contributes to the active power injection into the grid. Meanwhile, the BES dynamically compensates for the PV power fluctuations, thereby stabilizing the DC-link voltage and supporting the resiliency of the inverter under grid disturbances. In this structure, the PV ensures energy harvesting efficiency, while the BES–inverter enhances system stability and reliability.

E. System Functionality

Overall, the hybrid system forms a PV–Battery grid-forming unit. The inverter operates under grid-forming control, establishing voltage and frequency at the PCC, while the BES provides fast power compensation through the DC-link. The LC filter ensures power quality by suppressing harmonics, and the coordinated operation with the PV system enables reliable power supply under both grid-connected and weak-grid scenarios.

2.2. Conventional Control of the PV-BES GFM System

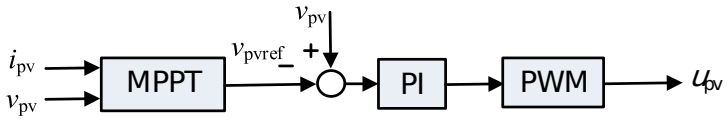

Fig. 2. Control diagram of the PV system control.

As shown in Fig. 2, a maximum power point tracking (MPPT) algorithm is employed to optimize the energy extraction of the PV array under fluctuating irradiance and temperature conditions. By continuously adjusting the operating point, the MPPT ensures maximum utilization of the available solar power. Among various approaches, the P&O MPPT method remains the most widely applied, owing to its simplicity, low computational effort, and straightforward implementation.

In the P&O scheme, voltage perturbations are periodically introduced into the PV terminal voltage, and the resulting change in output power is monitored to determine

the perturbation direction. Through this process, the reference voltage of the PV array is adaptively adjusted toward the maximum power point. A proportional–integral (PI) regulator then tracks this reference by minimizing the error between the actual and reference voltages. The regulated signal is further processed by a pulse-width modulation (PWM) unit to generate the duty cycle for the boost converter, thereby enabling the PV system to operate at the desired voltage and achieve optimal power delivery.

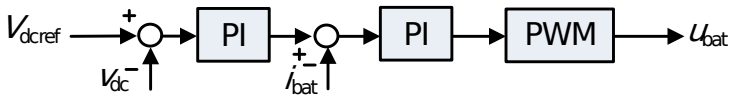

Fig. 3. Control diagram of the BES system.

In the BES system, a cascaded control structure with an outer voltage loop and an inner current loop is implemented, as illustrated in Fig. 3. The outer loop regulates the DC-link voltage by tracking the reference value V_{dcref}. Any deviation of the DC-link voltage from its setpoint is converted into a reference for the battery current. This reference is then forwarded to the inner current loop, which ensures accurate and fast tracking through high-bandwidth regulation. The inner loop directly controls the battery-side current, thereby providing fast dynamic response against disturbances.

It should be clarified that the slow layer in the proposed framework is not intended to implement a dedicated battery state-of-charge (SoC) management strategy, nor does it generate an explicit SoC-based or current reference for the DC–DC converter. Instead, the slow layer operates at the system-control level to shape the long-term energy exchange between the inverter and the battery by regulating DC-link energy dynamics and coordinating operating modes, thereby indirectly mitigating battery degradation.

Specifically, the slow layer performs two primary functions. First, it schedules energy-aware control parameters, such as virtual inertia and damping, based on DC-link energy deviation, with the objective of limiting large energy excursions and reducing unnecessary charge–discharge cycling. Second, it coordinates operating modes to avoid abrupt power transitions during GFL–GFM and grid-connected–islanded transitions. This design choice is intentional, as the DC-link represents the immediate energy interface between fast inverter dynamics and the battery in grid-forming PV–BES systems.

Regarding the DC–DC control structure shown in Fig. 3, the converter is designed to track a DC-link voltage reference, which is a widely adopted and practical architecture in hybrid PV–BES systems. Under this structure, the battery current is implicitly determined by the instantaneous power imbalance at the DC-link rather than by an externally imposed current or SoC reference. The proposed slow-layer mechanisms therefore act upstream of the DC–DC converter by reshaping inverter-side dynamics and mode transitions, rather than directly modifying the DC–DC control loop. As a result, the battery experiences smoother current profiles and reduced micro-cycling over time, even in the absence of an explicit SoC feedback loop.

This cascaded configuration effectively decouples the slow voltage dynamics from the faster current dynamics. The voltage loop guarantees the long-term balance of the DC-link energy, while the current loop maintains stability during fast transients. As a result, the BES is able to absorb or inject power promptly, which ensures stable energy exchange at the dc bus and improves the overall robustness of the grid-forming inverter under varying operating conditions.

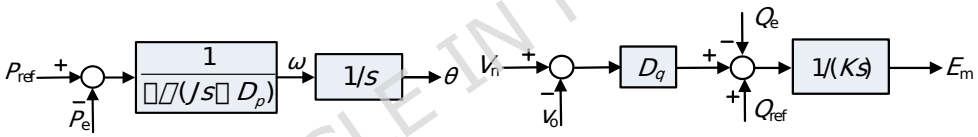

(a) (b)

Fig. 4. Virtual synchronous generator control block diagram: (a) active power control and (b) reactive power control.

The GFM inverter adopts a virtual synchronous generator (VSG) control scheme, allowing it to reproduce the electromechanical behavior of synchronous machines and deliver inertia and damping to the system. As depicted in Fig. 4, the VSG controller is structured into two coordinated parts: the active power control loop and the reactive power control loop, which can be detailed as follows.

$$J w_n \frac{dw}{dt} = P_{ref} - P_e + D_p(w - w_n) \tag{6}$$

$$E_m = \frac{1}{Ks}[(Q_{ref} - Q_e) + D_q(V_n - V_o)] \tag{7}$$

$$\Delta w = w - w_n \tag{8}$$

Here, P_{ref} and P_e denote the reference and measured active power, while ω_n and D_p represent the nominal angular frequency and the active power damping coefficient, respectively. Likewise, Q_{ref}, Q_e, D_q, K, V_n, and V_o correspond to the reference reactive

power, measured reactive power, reactive droop coefficient, reactive virtual inertia, nominal voltage, and the PCC voltage, respectively.

3. Proposed Multi-Timescale Energy-Aware GFM Control Strategy.

The proposed controller adopts a multi-timescale hierarchical structure that integrates energy awareness and adaptive virtual inductance to enhance both stability and transient performance. As illustrated in Fig. 5, the framework is organized into three layers coordinated by a supervisory mode manager.

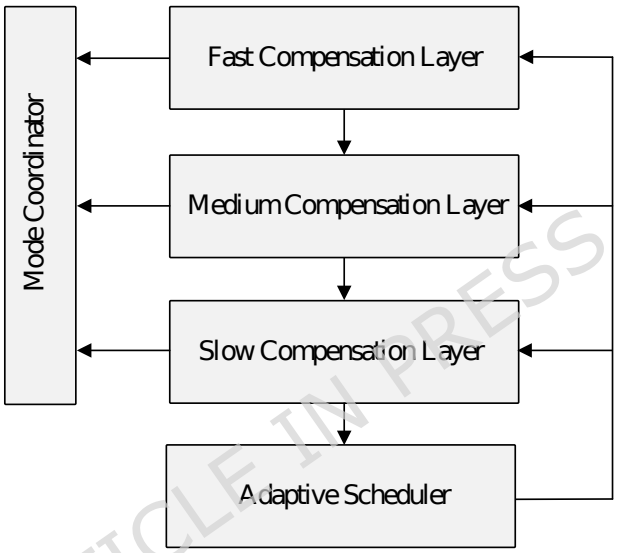

Fig.5. Block diagram of multi-timescale hierarchical structure.

3.1.Fast Compensation Layer

The innermost control layer is responsible for regulating the inverter output currents i_{dq} with a very short sampling period. A pair of PI controllers is implemented in the synchronous reference frame to eliminate steady-state errors and achieve accurate tracking of the reference currents. The control outputs are modulated using space vector PWM, which provides high utilization of the DC-link voltage and reduced harmonic distortion.

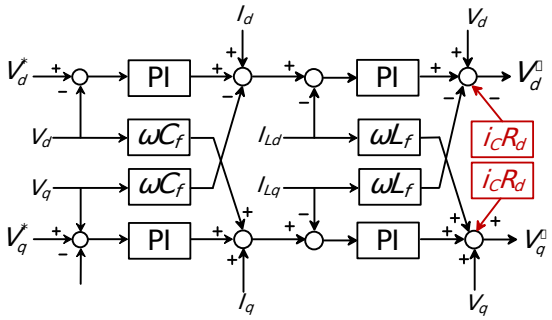

Fig.6. Block diagram of fast compensation layer control.

To further enhance stability, an active damping scheme is integrated into this layer. By injecting virtual resistance and compensating capacitor current feedback, the resonance peak of the LC filter is effectively suppressed without requiring additional passive components. This design prevents harmful oscillations and ensures stable operation even under weak grid conditions.

The fast layer guarantees rapid and robust current tracking, enabling the inverter to respond immediately to dynamic reference changes generated by the upper layers. In doing so, it forms the foundation of the multi-timescale control architecture, providing high-frequency stability and ensuring reliable interaction with both the grid and the local energy storage system.

3.2. Power Control

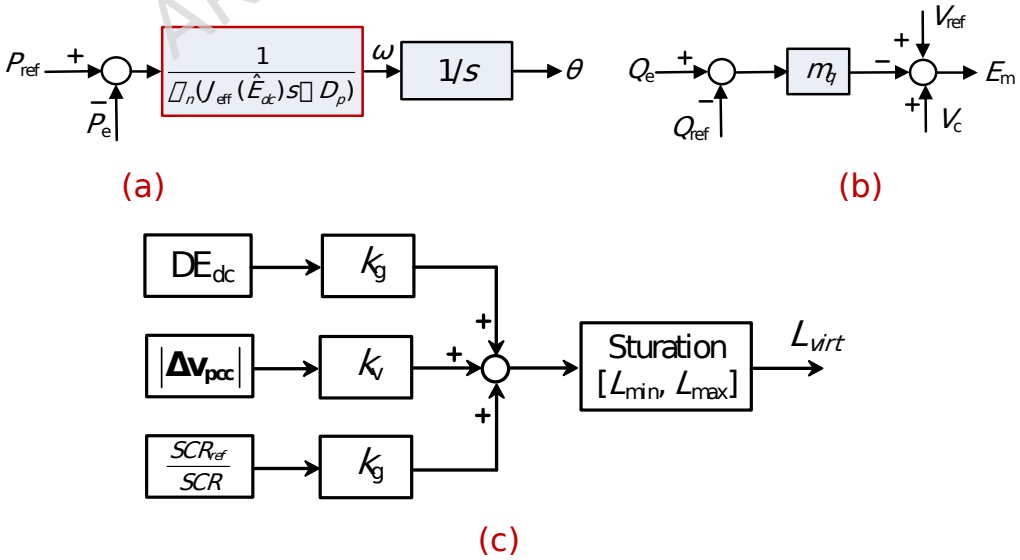

Fig. 7. Improved virtual synchronous generator control block diagram: (a) active power control and (b) reactive power control.

As shown in Fig. 7, the power control layer is constructed on the principle of a VSG, which emulates the inertial and damping characteristics of conventional synchronous machines. In this framework, the inverter autonomously generates the frequency reference ω and the voltage reference V^* according to the active and reactive power control loops. The dynamic equations are expressed as

$$\dot{\omega} = \frac{P_{ref} - P_e - D_p \Delta\omega}{J_{eff}(\hat{E}_{dc})}, \qquad V^* = V_{ref} - m_q(Q_e - Q_{ref}), \tag{9}$$

where P_{ref} and Q_{ref} are the active and reactive power references, P_e and Q_e are the measured outputs, D_p is the active power damping factor, and m_q is the reactive power droop coefficient. Notably, $J_{eff}(\hat{E}_{dc})$ denotes the energy-aware virtual inertia, which is adaptively scheduled by the slow layer according to the estimated DC-link energy $\hat{E}_{dc}$.

By dynamically tuning the effective inertia, the controller can provide stronger frequency support when sufficient DC-link energy is available, and operate more conservatively when energy is scarce, thereby avoiding instability and over-damping. This design enhances the system's frequency damping capability, ensures flexible voltage regulation, and significantly improves the resilience of the inverter under disturbances such as sudden load changes, weak-grid conditions, or mode transitions. Compared with conventional VSG implementations using fixed inertia parameters, the proposed approach prevents performance degradation across varying operating conditions, achieving both improved adaptability and robustness.

The virtual inductance L_{virt} is implemented by adding a differential compensation term proportional to the derivative of the output current, thereby shaping the inverter's output impedance to enhance stability under weak-grid conditions. The compensation gains introduced in (11) are incorporated into the damping and inertia scheduling path, enabling dynamic adjustment of the equivalent swing-response parameters. The coefficients Dc and ωf are selected based on small-signal sensitivity analysis to ensure adequate damping and suitable bandwidth for the adaptive mechanism. Their final values are listed in Table 1 for reproducibility.

3.3. Slow Adaptation Control and Adaptive Scheduler

At the outermost layer, the controller incorporates a slow compensation mechanism to capture long-term variations in both the internal energy state and external grid conditions. A DC-link energy observer is employed to estimate the stored energy as

$$\hat{E}_{dc} = \frac{1}{2} C_{dc} v_{dc}^2, \tag{10}$$

which reflects the instantaneous capability of the inverter to provide inertial and damping support. In parallel, a grid-strength estimator derives the short-circuit ratio (SCR), serving as an online indicator of system strength and external disturbance resilience.

As shown in Fig. 7 (c), based on these two indicators, the adaptive scheduler dynamically updates the virtual inductance and damping-related parameters in real time. The scheduling law is expressed as

$$L_{\text{virt}} = \text{sat}\left(L_0 + k_e |\Delta E_{dc}| + k_v |\Delta v_{PCC}| + \frac{k_g}{\text{SCR}} \right), \tag{11}$$

where L0 is the nominal virtual inductance, k_e, k_v, and k_g are tuning coefficients, and the saturation function ensures that L_{virt} remains bounded within a feasible range $[L_{\min}, L_{\max}]$.

Similarly, the energy-damping compensation gains are adjusted by

$$i_{d,\text{comp}} = D_c \text{HPF}_{w_f}(\Delta E_{dc}), \qquad i_{q,\text{comp}} = K_v \Delta v_{PCC}, \tag{12}$$

where the coefficients D_c and ω_f are also scheduled by the slow layer according to $\hat{E}_{dc}$ and SCR.

To explicitly define the energy-aware inertia adaptation, the effective virtual inertia is scheduled as

$$J_{eff}(E_{dc}) = J_0 \left[1 + k_E \times \text{sat}\left(\frac{E_{dc} - E_{dc,ref}}{E_{dc,ref}} \right) \right] \tag{13}$$

where J_0 is the nominal virtual inertia, E_{dc} is the estimated DC-link energy, $E_{dc,ref}$ denotes its nominal value, and k_E is the energy-sensitivity coefficient. The saturation function limits the inertia variation within a predefined range to ensure stability and avoid excessive parameter excursions.

It is important to note that the adaptive inertia is not intended to continuously vary under nominal operating conditions. When DC-link energy fluctuations are effectively suppressed, the proposed scheduling law naturally keeps the inertia close to its nominal

value. This behavior indicates stable operation rather than a lack of influence of the adaptive mechanism.

The results in Fig. 12 show very small DC-link voltage deviations under the proposed control strategy. This outcome should be understood as the combined effect of multiple coordinated mechanisms acting at different timescales. The adaptive virtual inductance and energy-aware damping primarily act on fast electrical dynamics and directly suppress inverter–grid oscillations, which leads to reduced DC-link energy ripple. The adaptive inertia, by contrast, plays a preventive and supervisory role: it reshapes the frequency–power dynamics when larger energy excursions occur, particularly under severe disturbances or weak-grid conditions, thereby preventing the system from entering operating regimes associated with excessive DC-link energy deviations.

In other words, the adaptive inertia does not primarily minimize small-signal DC-link ripple during normal operation. Instead, it ensures robustness by constraining the system response under adverse conditions. Once stability is achieved and DC-link energy fluctuations are limited, the inertia remains close to its nominal value by design, while still being essential for maintaining stability margins and preventing large-scale energy stress.

The effective inertia term $J_{eff}(E_{dc})$ is derived from the linearization of the DC-link energy dynamics around the nominal equilibrium point. It is formulated as a monotonic function of the available capacitor energy so that higher E_{dc} enables a more dynamic response, while lower E_{dc} necessitates conservative behavior. In addition, the influence of the sign of the DC-link voltage deviation is incorporated in the scheduling mechanism, allowing the controller to respond more aggressively to overvoltage events even under low-energy conditions, while protecting the system during undervoltage scenarios. This ensures that Jeff captures both the energy level and the physical direction of the disturbance.

The SCR is estimated online using a frequency-domain impedance identification approach based on naturally occurring perturbations in the inverter output current as

$SCR = V_{grid} / \omega L_{grid}$. By measuring the PCC voltage and current and applying a least-squares fitting algorithm, the grid inductive reactance is obtained and converted to the corresponding SCR value. A low-pass filter is used to suppress noise while preserving meaningful variations in grid strength, ensuring robust medium-timescale adaptation.

Through this adaptive law, the slow layer provides supervisory capability to balance stability enhancement and dynamic responsiveness. In weak-grid scenarios or under depleted DC-link energy, the scheduler increases L_{virt} and compensation gains to ensure robustness; under strong-grid conditions with abundant energy, it relaxes these parameters to reduce conservatism and improve efficiency. Compared with conventional fixed-parameter approaches, this design enables greater adaptability, robustness, and resilience across diverse operating conditions.

3.4 Explicit Formulation of the Proposed Controller

To explicitly illustrate the implementation of the proposed energy-aware GFM controller, the inverter voltage reference is formulated as

$$v_{inv}^{*} = v_{VSG} - L_{virt}(t)\frac{di_f}{dt} - R_{virt} i_f \quad (14)$$

where $\mathbf{v}_{VSG}$ is the voltage reference generated by the VSG-based power control loop, $L_{virt}(t)$ is the adaptive virtual inductance scheduled by the energy-aware slow layer, and the derivative term represents the compensation current injected to reshape the inverter output impedance. In practice, the derivative term is implemented using filtered current feedback, and all adaptive parameters are subject to saturation and rate limits to ensure numerical robustness.

For comparison, the benchmark controller adopts a conventional fixed-parameter VSG structure without adaptive virtual inductance or compensation current injection. The inverter voltage reference is given by

$$v_{inv,bench}^{*} = v_{VSG} \quad (15)$$

Unlike the proposed controller, the benchmark formulation does not include virtual inductance adaptation or current compensation terms.

3.5. Mode Coordination

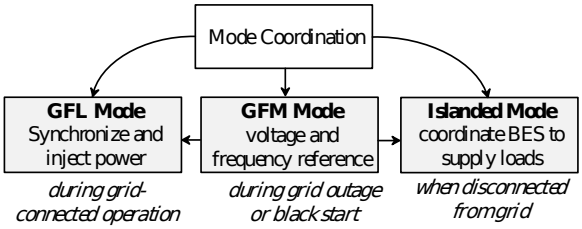

Fig. 8. Supervisory mode coordination framework of the PV–BES system, illustrating the transition logic among grid-following (GFL), grid-forming (GFM), and islanded operation modes under grid-connected, grid-outage, and islanded conditions.

To support flexible operation under diverse grid conditions, a supervisory mode coordinator is implemented to manage the transitions among grid-forming, grid-following, and islanded modes. The coordinator continuously monitors system indicators such as PCC voltage magnitude, frequency deviation, PLL lock status (for GFL operation), and DC-link stability. Based on these signals, a hysteresis-based switching logic is applied to avoid frequent toggling between modes and to guarantee smooth handover of control objectives. As shown in Fig. 8, the proposed controller explicitly injects the adaptive virtual inductance and compensation current terms into the current control loop, whereas these paths are absent in the benchmark controller.

It is noted that the distinction between grid-following (GFL), grid-forming (GFM), and islanded modes is introduced to reflect practical operating conditions rather than to define independent control strategies. The proposed energy-aware GFM controller is activated whenever the inverter is required to establish voltage and frequency references.

The transition between GFL and GFM modes is governed by grid-condition indicators, including the PCC voltage magnitude, frequency deviation, and grid availability. Under normal grid-connected conditions with a sufficiently strong grid, the inverter operates in GFL mode to synchronize with the grid and inject power efficiently. When grid strength deteriorates, such as under weak-grid conditions, grid outages, or black-start scenarios, the control is switched to GFM mode, in which the inverter autonomously establishes the voltage and frequency at the PCC. A hysteresis-based switching logic is adopted to prevent frequent mode toggling and to ensure smooth transitions.

The islanded mode represents a special operating condition in which the inverter supplies local loads without grid support. While islanded operation is not the main focus

of this work, it is inherently a grid-forming scenario. In islanded mode, the same energy-aware inertia and adaptive virtual inductance mechanisms remain active, enabling stable voltage and frequency regulation under load variations.

From the perspective of the proposed contribution, the inclusion of GFL and islanded modes does not introduce additional control objectives. Instead, it demonstrates that the proposed energy-aware GFM controller can be seamlessly embedded into a practical PV–BES system that operates across multiple grid conditions. The mode coordination mechanism ensures that transitions among operating modes do not violate the assumptions underlying the proposed GFM control, thereby preserving stability and performance.

During a mode transition, the coordinator ensures that the internal states of the control loops—such as current references, frequency, and voltage set-points—are gradually adjusted to prevent transients. In addition, a current limiting mechanism is integrated into the coordinator to cap the inverter output under abnormal or fault conditions, thereby ensuring device protection and maintaining system safety.

The proposed multi-timescale control framework, combined with the mode coordinator, allows the inverter to adaptively reshape its dynamic characteristics according to both the internal energy state and the external grid strength. This capability provides improved stability margins, faster transient response, and enhanced robustness under weak-grid conditions, fault disturbances, and mode-switching scenarios, thereby extending the applicability of the proposed strategy to real-world PV–battery hybrid systems and resilient microgrids.

This section has presented a multi-timescale energy-aware grid-forming (GFM) control strategy that integrates fast compensation, power control, slow adaptation, and mode coordination into a unified framework. At the innermost layer, the fast current control with active damping ensures high-bandwidth regulation and suppresses resonance, providing a stable foundation for the system. The medium layer, based on a VSG model, generates frequency and voltage references while embedding energy-aware inertia and damping characteristics, thereby enhancing transient performance under power disturbances. At the outermost layer, the slow compensation mechanism continuously observes the DC-link energy and estimates the grid strength, adaptively scheduling the virtual inductance and compensation gains to guarantee robustness across a wide operating envelope. Finally, the supervisory mode coordinator manages

seamless transitions among GFM, GFL, and islanded modes, with built-in current limiting to ensure protection during abnormal conditions.

By combining these layers, the proposed strategy achieves a coordinated balance between fast dynamic response and long-term robustness, enabling the inverter to operate stably under weak-grid conditions, during mode switching, and against sudden disturbances. Compared with conventional fixed-parameter GFM controllers, the proposed framework provides greater adaptability, improved damping, and enhanced resilience, making it particularly suitable for PV–battery hybrid systems and emergency mobile power applications.

For clarity, the functional roles of the fast, medium, and slow compensation layers are summarized here. The fast layer operates on the millisecond timescale and is responsible for stabilizing grid-forming dynamics through virtual inductance shaping and damping injection, providing immediate suppression of low-frequency oscillations under weak-grid conditions. The medium layer adapts the virtual inertia and damping coefficients based on the estimated DC-link energy and SCR, enabling the inverter to autonomously reshape its dynamic response as grid strength varies. The slow layer governs long-term energy scheduling and battery stress mitigation, ensuring that changes in operating conditions do not cause excessive cycling or degradation. Together, these layers form a coherent multi-timescale structure in which rapid stabilization, dynamic parameter adaptation, and lifetime-aware energy management operate in a coordinated manner.

The mode coordination mechanism is not merely an engineering implementation step but plays a critical role in ensuring consistency within the multi-timescale adaptive control structure. Uncoordinated transitions among MPPT, charging, and GFM modes can induce abrupt variations in DC-link energy, violating the assumptions underlying the adaptive inertia and damping scheduling. The coordinator ensures mathematically smooth transitions by aligning energy trajectories and preventing discontinuities in control gains, thereby preserving stability during mode switching under weak-grid conditions.

4 Stability Analysis and Battery Lifetime Modeling.

In addition to the small-signal stability analysis, a battery lifetime model is incorporated to evaluate the long-term impact of the proposed controller. The model

includes both cycle-aging and calendar-aging mechanisms, where cycle degradation is quantified via rainflow-based depth-of-discharge (DoD) analysis and current-rate dependence, while calendar aging reflects capacity fade under sustained voltage and temperature conditions. This framework enables assessment of how reductions in DC-link energy ripple and transient power stress contribute to extended battery lifetime. Lithium-ion battery degradation is commonly described by two components: calendar aging and cycle aging. Calendar aging reflects the gradual capacity loss during storage and is modeled as a linear function of the operating time, expressed as ($Q_{cal}(t) = k_{cal} t$), where k_{cal} is the empirical aging coefficient. Cycle aging, on the other hand, is caused by repetitive charge–discharge cycling, and its severity depends on the depth-of-discharge (DoD), current rate, and cumulative number of cycles. A semi-empirical power-law model is adopted to represent this mechanism: $Q_{cyc} = k_{cyc}(N/1000)^{0.7}$, where kcyc is the cycle-aging coefficient and N denotes the accumulated equivalent full cycles (EFC). The EFC is computed from the DC-link energy fluctuations induced by inverter–grid interactions, such that stronger oscillations produce larger EFC values and hence accelerated battery degradation. By combining both aging mechanisms, the remaining battery capacity is written as $Q_{rem} = 1 - Q_{cal} - Q_{cyc}$. This formulation enables the subsequent analysis in Section 5, where the proposed controller—through the suppression of DC-link energy ripple—significantly reduces the EFC accumulation rate. As a result, the long-term degradation is mitigated, which is further demonstrated by the comparative lifetime curves shown in Figures 18 and 19.

4.1. Stability Analysis

To investigate the small-signal stability of the proposed control, an inverter with LC filter and virtual synchronous generator control is modeled in the synchronous dq reference frame.

(1) LC filter dynamics

The inverter-side effective inductance includes both the physical filter inductance L_f and the adaptive virtual inductance L_{virt}:

$$L_f^{\text{eff}} = L_f + L_{\text{virt}}. \tag{16}$$

The inverter current dynamics are expressed as

$$L_f^{\text{eff}} \frac{di_{fd}}{dt} = v_{inv,d} - v_{cd} - R_f i_{fd} + \omega_0 L_f^{\text{eff}} i_{fq}, \tag{17}$$

$$L_f^{\text{eff}} \frac{di_{fq}}{dt} = v_{inv,q} - v_{cq} - R_f i_{fq} - \omega_0 L_f^{\text{eff}} i_{fd} \tag{18}$$

where i_{fd} and i_{fq} denote the inverter filter currents in the d and q axes, respectively; $v_{\text{inv,d}}$, $v_{\text{inv,q}}$ are the inverter output voltages; v_{cd}, v_{cq} are the capacitor voltages; and R_{f} is the series resistance of the inductor.

The capacitor dynamics are given by

$$C_f \frac{dv_{cd}}{dt} = i_{fd} - i_{gd} + \omega_0 C_f v_{cq} \tag{19}$$

$$C_f \frac{dv_{cq}}{dt} = i_{fq} - i_{gq} - \omega_0 C_f v_{cd} \tag{20}$$

where i_{gd}, i_{gq} represent the grid-side currents exchanged with the utility grid through the PCC capacitor, and C_{f} is the filter capacitor.

(2) Inner current control loop

The current references are tracked using PI regulators:

$$v_{inv,d} = k_{p,i}(i_d^* - i_{fd}) + k_{i,i} x_d, \; v_{inv,q} = k_{p,i}(i_q^* - i_{fq}) + k_{i,i} x_q \tag{21}$$

where i_{d}*, i_{q}* are the reference currents, x_d, x_q are the integrator states, and $k_{p,i}, k_{i,i}$ are the proportional and integral gains of the PI controller.

(3) VSG-based outer-loop dynamics

The VSG emulates virtual inertia and damping:

$$J_{\text{eff}} \frac{d\omega}{dt} = P^* - P - D_p(\omega - \omega_0), \; \frac{d\delta}{dt} = \omega - \omega_0, \tag{22}$$

where J_{eff} is the energy-aware virtual inertia adaptively scheduled by the proposed control based on the DC-link energy; D_{p} is the damping coefficient; ω and δ are the inverter angular frequency and phase angle; ω_0 is the nominal angular frequency; and P*, P are the active power reference and measured active power.

The small-signal perturbations of active and reactive power can be expressed as

$$\Delta P \approx 1.5 V_{d0} \Delta i_{fd} + 1.5 I_{d0} \Delta v_{cd}, \; \Delta Q \approx -1.5 V_{d0} \Delta i_{fq}, \tag{23}$$

where V_{d0} and I_{d0} are the steady-state d-axis voltage and current.

(4) State-space representation

By linearizing the above dynamics around an equilibrium point, the state vector is defined as

$$\Delta x = [\Delta i_{fd}, \Delta i_{fq}, \Delta v_{cd}, \Delta v_{cq}, \Delta w, \Delta d, \Delta x_d, \Delta x_q]^{\bullet} . \tag{24}$$

The linearized system can be expressed as

$$\Delta \dot{x} = A \Delta x, \tag{25}$$

where the system matrix A is a function of the effective inductance L_f^{eff}, the adaptive inertia J_{eff}, and the short-circuit ratio that reflects grid strength. The eigenvalues of A reveal the local stability margin of the closed-loop system.

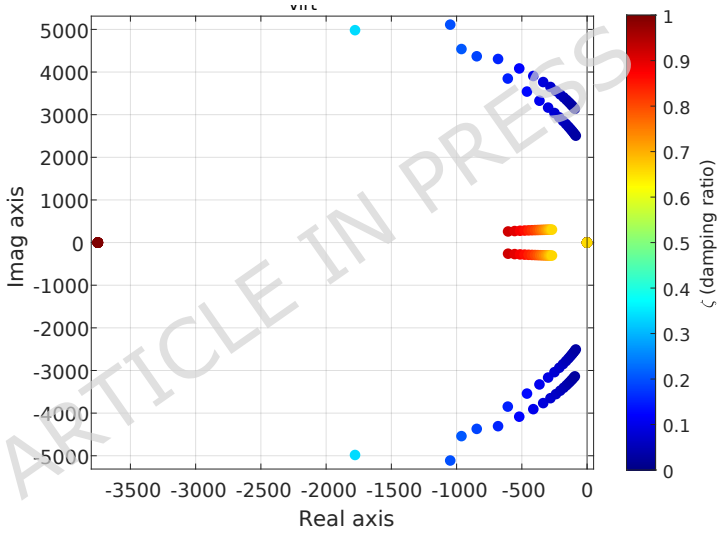

Fig. 9. Eigenvalue loci under varying virtual inductance L_{virt} (with fixed J_{eff}=0.4, SCR = 1.5)

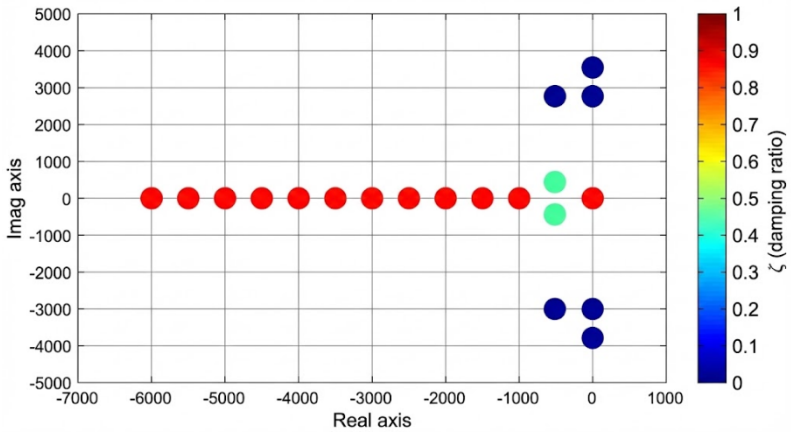

Fig. 10. Eigenvalue loci under varying effective inertia J_{eff} (with fixed L_{virt}=15 mH, SCR = 1.5)

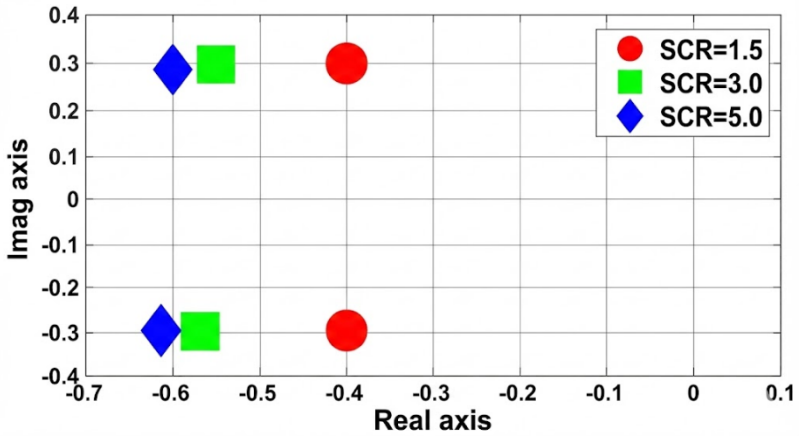

Fig. 11. Eigenvalue distribution under different grid strengths (SCR = 1.5, 3, and 5, with fixed L_{virt} = 15 mH, J_{eff} = 0.4)

Fig. 9 illustrates the eigenvalue loci under varying virtual inductance L_{virt} while keeping J_{eff} =0.4 and SCR = 1.5. As L_{virt} increases, the dominant poles initially move further into the left-half plane, indicating improved damping of oscillatory modes. However, when L_{virt} becomes excessively large, the poles tend to bend back towards the imaginary axis, which reduces the damping ratio and slows down the transient response. This demonstrates the existence of an optimal range of L_{virt} that balances stability and dynamic performance.

Fig. 10 shows the eigenvalue loci under varying effective inertia J_{eff} with fixed L_{virt} =15 mH and SCR = 1.5. It is observed that increasing J_{eff} shifts the electromechanical poles towards lower frequencies, thereby slowing the system dynamics. A moderate inertia improves frequency stability by suppressing rapid oscillations, whereas an excessively high inertia reduces damping and causes the poles to cluster closer to the imaginary axis. This confirms that inertia scheduling is necessary to maintain an adequate stability margin.

Fig. 11 presents the eigenvalue distribution under different grid strengths (SCR = 1.5, 3, and 5) with fixed L_{virt} =15 mH and J_{eff} =0.4. Under weak grid conditions (SCR = 1.5), the dominant poles shift towards the right-half plane, indicating reduced damping and a smaller stability margin. As the grid strength increases (SCR = 3 and 5), the poles move deeper into the left-half plane, reflecting enhanced stability and faster oscillation

decay. This comparison highlights the effectiveness of adaptive control in compensating for weak-grid scenarios.

5. Simulation Results

To enhance the transparency and reproducibility of the numerical evaluation, a detailed description of the simulation setup is provided here. All simulations are carried out in MATLAB/Simulink using a high-fidelity switching model of a two-level voltage-source inverter. Device-level nonidealities, including switching delay, dead-time, on-state voltage drop, and parasitic capacitances, are incorporated to capture realistic transient behaviors. The grid is represented by a frequency-dependent Thevenin equivalent corresponding to the desired SCR conditions. The battery is modeled using a second-order RC equivalent circuit with SoC-dependent characteristics, ensuring that the DC-link energy interacting with the proposed controller reflects practical battery dynamics. A fixed-step solver (ode23tb) is used with a maximum step size of 2 μs, a switching frequency of 10 kHz, and an inner-loop sampling rate of 50 kHz. This setup ensures accurate representation of the GFM dynamics and allows fair comparison between the proposed adaptive method and conventional fixed-parameter control.

Table 1. Control parameters of the system referring to Figure 1.

Parameter	Value	Parameter	Value
$V_{dc,ref}$	700 V	L_f	5 mH
S_N	5 kVA	C_f	15 μF
P_{ref}	5 kW	L_g	9.2 mH
Q_{ref}	0 VAr	R_g	0.25 Ω
C_{dc}	1100 μF	D_p	1600
J	0.4 kg·m²	D_q	25
D_c	8	L_{virt}	3 mH
w_f	20 rad/s	D_v	0.15
w_n	2π·50 rad/s	w_{LPF}	250 rad/s
k_p^w	0.8	k_i^w	50
k_p^v	0.15	k_i^v	15
R_f	0.1 Ω	Rdc	0.05 Ω
x	0.707	SCR	2.5 (weak grid)

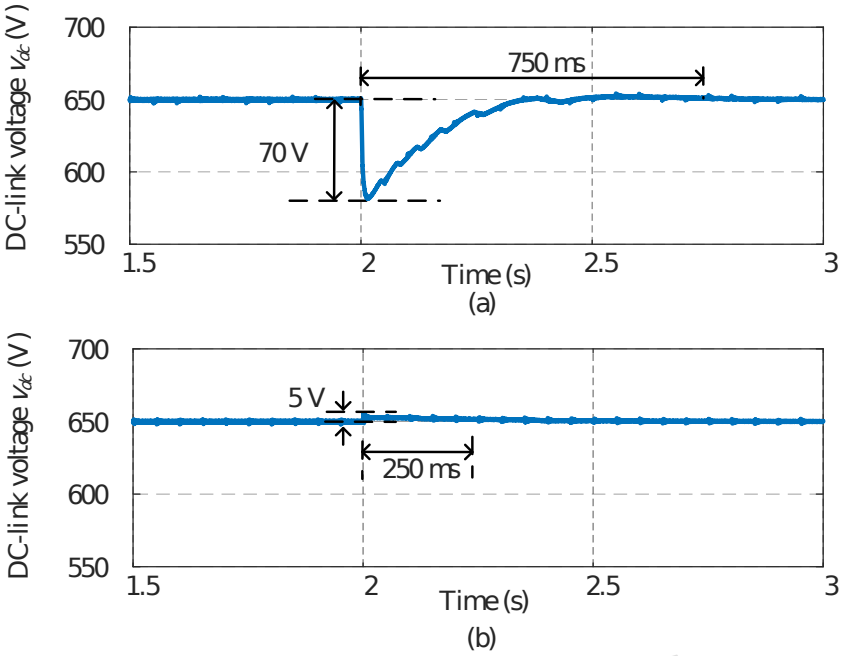

Figure 12. DC-link voltage responses under irradiance variation: (a) conventional VSG control; (b) proposed CTEA-GFM control.

Figure 12 shows the DC-link voltage responses under irradiance variation. In the case of conventional VSG control Fig. 12(a), the sudden power fluctuation results in a significant DC-link voltage dip of about 70 V and a long recovery time of nearly 750 ms, which may deteriorate system stability. By contrast, with the proposed CTEA-GFM control Fig. 12(b), the DC-link voltage deviation is effectively suppressed within only 5 V, and the recovery time is shortened to around 250 ms. These results demonstrate the superior capability of the proposed method in maintaining DC-link stability under irradiance disturbances. For clarity and reproducibility, the applied disturbance signal is explicitly defined. In the weak-grid transient case, a 0.25 p.u. active-power step is applied at the PCC at the specified time instant. The same disturbance profile is used for both the benchmark and proposed controllers to ensure a fair comparison.

Figure 13 illustrates the active and reactive power responses at the PCC under the same irradiance variation. With conventional VSG control Fig. 13(a), both active and reactive powers experience large oscillations, reaching up to 600 W and 500 Var, respectively. Under the proposed CTEA-GFM control Fig. 13(b), these oscillations are almost eliminated, and the power remains smooth and stable. This indicates that the proposed strategy not only improves DC-link voltage regulation but also significantly enhances power quality at the PCC.

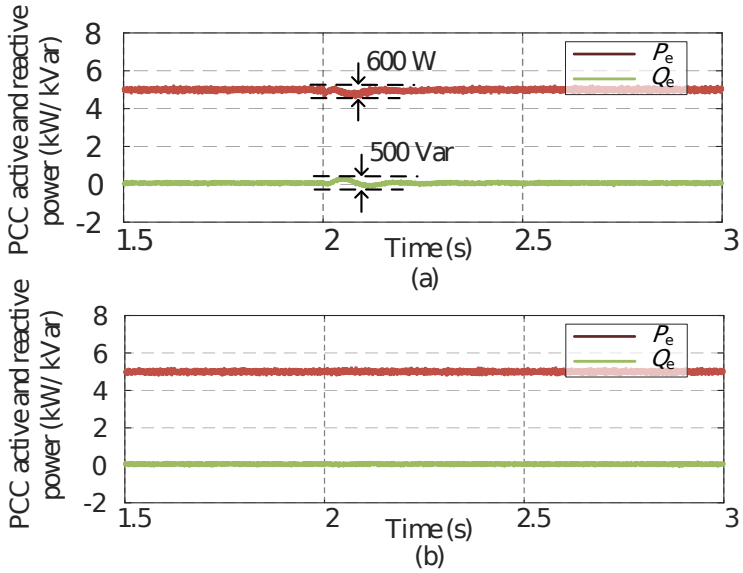

Figure 13. Active and reactive power responses at the PCC under irradiance variation: (a) conventional VSG control; (b) proposed CTEA-GFM control.

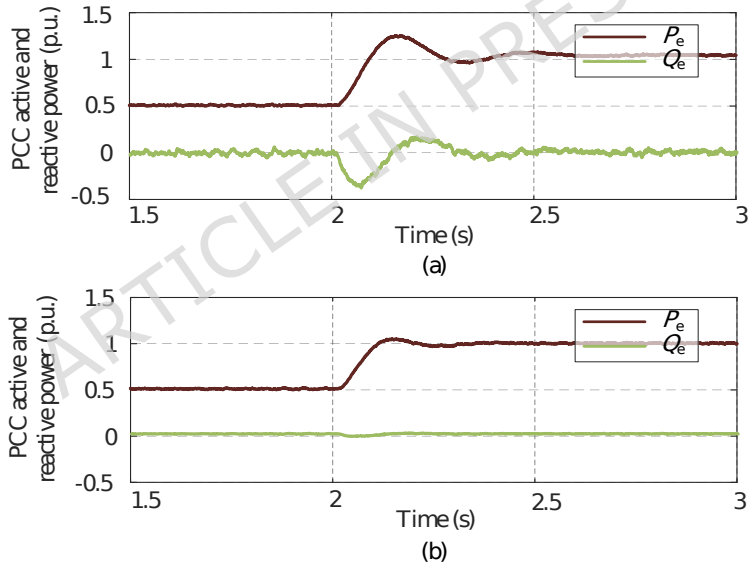

Figure 14. Transient responses of active and reactive power at the PCC. (a) Conventional control. (b) Proposed CTEA-GFM control.

Figure 14 shows the transient responses of active and reactive power at the PCC under irradiance variation. With conventional control Fig. 14(a), both P_e and Q_e exhibit significant overshoots and oscillations, leading to poor power quality. In contrast, under the proposed CTEA-GFM control Fig. 14(b), the active and reactive powers rapidly converge to their steady-state values with negligible oscillations, confirming the

superior capability of the proposed strategy in suppressing disturbances and stabilizing power exchange with the grid.

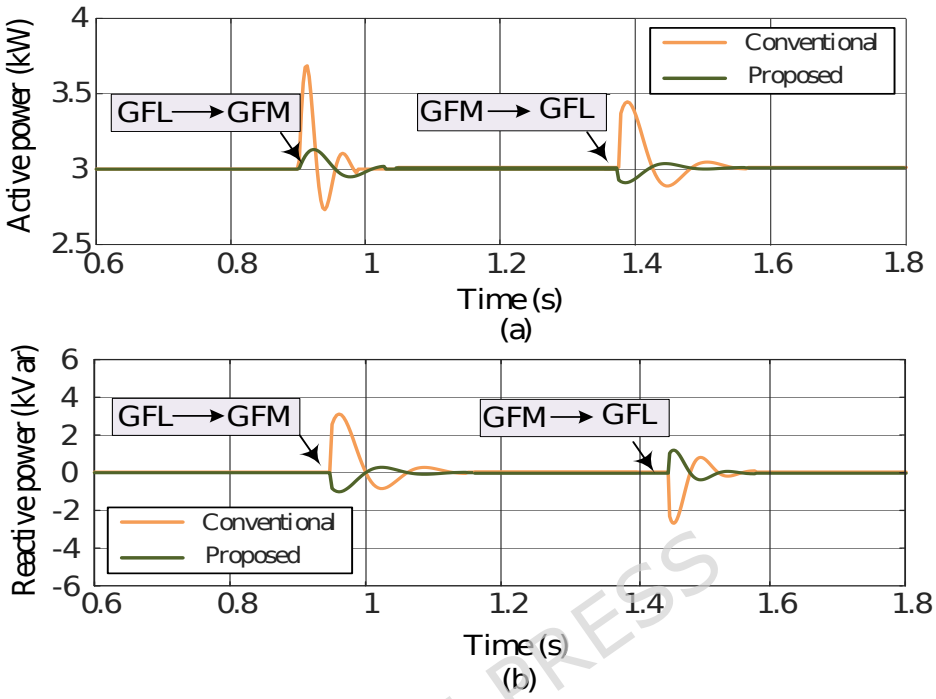

Figure 15. Active and reactive power responses during GFL–GFM–GFL mode transitions: (a) Conventional control. (b) Proposed CTEA-GFM control.

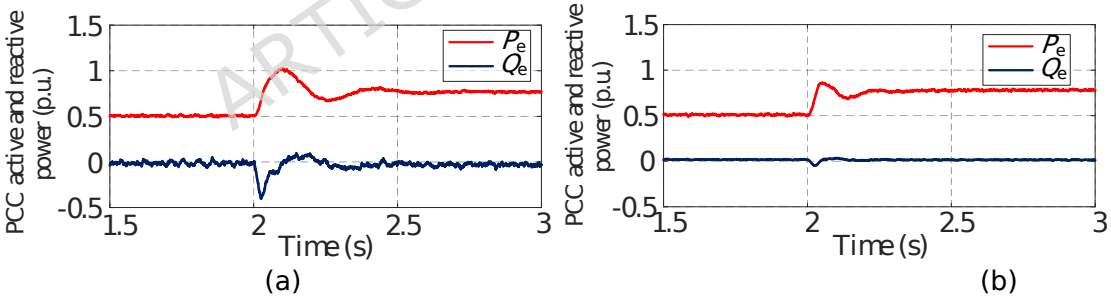

Figure 16. Transient responses of the PV-BES GFM system during the frequency disturbance. (a) Conventional fixed-parameter VSG control. (b) Proposed adaptive energy-aware VSG control.

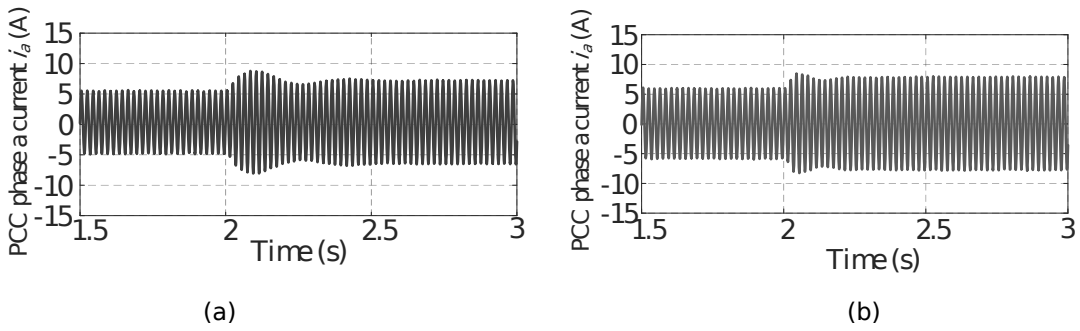

Figure 17. PCC phase-a current responses during the frequency disturbance. (a) Conventional method. (b) Proposed adaptive energy-aware VSG control.

Figure 15 illustrates the active and reactive power responses during GFL–GFM–GFL mode transitions. Under conventional control Fig. 15(a), the mode switching process induces severe oscillations in both active and reactive powers, with large overshoots and prolonged settling times. By comparison, the proposed CTEA-GFM control Fig. 15(b) ensures much smoother transitions, effectively limiting power fluctuations and enabling seamless switching between grid-forming and grid-following operations. These results demonstrate the robustness of the proposed control in handling dynamic operating scenarios. Although the results in Fig. 12–Fig. 15 mainly focus on DC-link voltage and power-flow fluctuations, this does not imply that the proposed controller is less involved in AC-side voltage and frequency regulation. In the proposed framework, the grid-forming (GFM) function is still realized through the VSG-based voltage and frequency control loop, while the additional compensation mechanisms primarily reshape fast electrical dynamics associated with inverter–grid interaction.

To verify that the grid-forming performance is not compromised, the PCC voltage magnitude and inverter frequency responses under the same disturbance scenarios are also examined. The results show that the proposed controller maintains stable PCC voltage and frequency regulation during disturbances, with dynamic performance comparable to, and in some cases improved over, the benchmark controller. This confirms that the enhanced DC-link stabilization is achieved without weakening the AC-side grid-forming capability.

As shown in Fig. 16, a 0.25 p.u. active-power step is applied to evaluate the transient performance of the PV–BES GFM system under a weak-grid condition. Under the conventional fixed-parameter VSG control, both the active and reactive power exhibit pronounced oscillations following the disturbance, and the settling process is noticeably slow due to insufficient damping. In contrast, the proposed CTEA-GFM control demonstrates a significantly more stable response. The adaptive adjustment of virtual inertia and damping, driven by the DC-link energy state, suppresses the oscillatory behavior and accelerates the transient settling. These results indicate that the proposed control strategy effectively enhances dynamic stability during sudden power-demand variations.

Figure 17 further illustrates the corresponding PCC phase-a current waveforms during the same 0.25 p.u. active-power step disturbance. Under the conventional VSG control, the current exhibits high-frequency oscillations with increased amplitude following the disturbance, indicating weakened damping and stronger inverter–grid interaction. With the CTEA-GFM GFM control, the current ripple and oscillatory components are substantially reduced, demonstrating improved current quality and more robust disturbance rejection. The smoother current profile confirms that the adaptive virtual impedance and energy-dependent damping effectively mitigate weak-grid oscillatory modes.

It should be emphasized that the battery degradation analysis presented in this work is based on a comparative and semi-empirical framework, rather than on detailed electrochemical battery modeling. Rainflow counting is employed as a standard cycle-counting technique to quantify the equivalent full cycles (EFC) induced by energy fluctuations, which is a widely adopted approach in battery aging analysis. In this study, rainflow counting is applied to the DC-link energy deviation trajectory, which serves as a proxy for the battery charge–discharge behavior through the DC–DC converter.

The DC-link ripple factor is introduced as a normalized indicator to characterize the amplitude of DC-link energy oscillations around the nominal operating point. Larger DC-link voltage or energy ripple implies stronger and more frequent compensation actions by the battery to maintain DC-link voltage regulation. These compensation actions directly translate into increased battery current fluctuations, which are used as the input for the rainflow counting algorithm. As a result, a higher DC-link ripple factor leads to a larger number of accumulated equivalent full cycles, establishing a direct correspondence between short-timescale inverter dynamics and long-term battery cycling stress.

The effect of DC-link voltage ripple on battery current is quantified through the power balance enforced by the DC–DC converter. The converter is assumed to regulate the DC-link voltage by absorbing or injecting power from the battery. Under this assumption, deviations in DC-link voltage and energy are directly associated with variations in battery current. Consequently, suppressing DC-link voltage and energy ripple reduces high-frequency battery current components and limits unnecessary micro-cycling, which is the dominant contributor to cycle aging in grid-forming battery energy storage applications.

For long-term degradation estimation, the battery aging model is intentionally kept semi-empirical and comparative. Both calendar aging and cycle aging are described using widely accepted power-law formulations, under the assumptions of constant operating temperature, fixed DC–DC converter efficiency, and identical operating conditions for both the benchmark and proposed control strategies. The objective of this analysis is not to predict the absolute battery lifetime, but to provide a fair relative comparison of degradation trends under different grid-forming control schemes.

The DC-link capacitance and DC–DC converter parameters are assumed to be fixed and identical across all compared cases. The DC-link capacitance determines the baseline energy buffering capability, while the DC–DC converter control ensures instantaneous power balance between the battery and the inverter. Their influence is therefore implicitly reflected in the DC-link energy dynamics. The proposed control strategy does not modify hardware parameters, but mitigates battery degradation by reshaping inverter-side dynamics and suppressing DC-link energy ripple under identical hardware and control configurations.

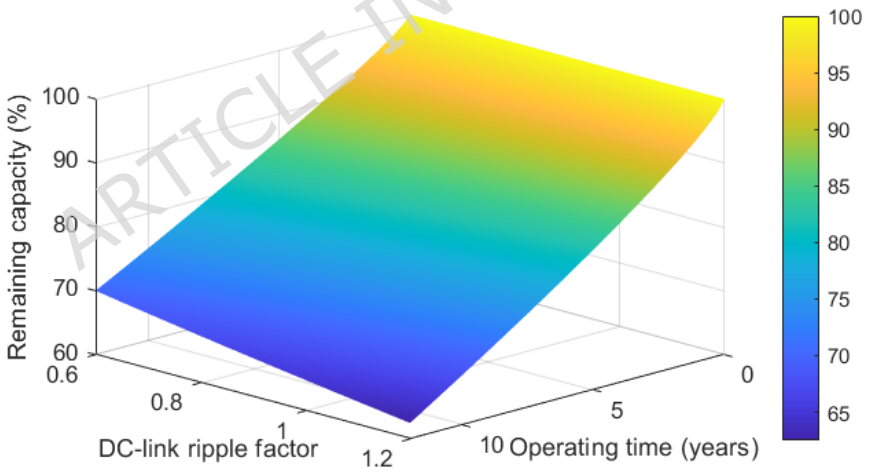

Figure 18. Remaining battery capacity as a function of operating time and DC-link ripple factor.

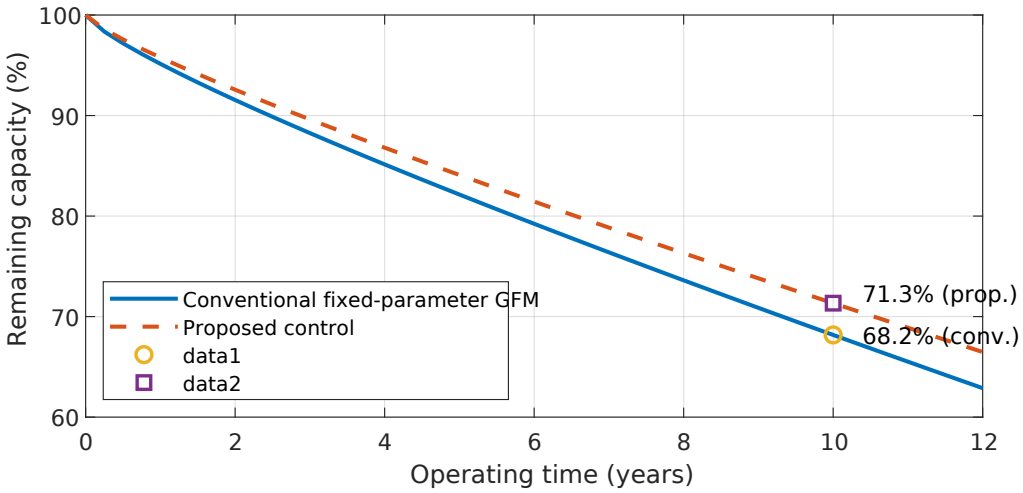

Figure 19. Comparison of remaining battery capacity under different GFM control strategies.

Figure 18 illustrates the combined influence of operating time and DC-link energy ripple on the remaining battery capacity. The DC-link ripple factor is defined as a normalized index reflecting the magnitude of energy oscillations around the nominal operating point. As the ripple factor increases from 0.6 to 1.2, the surface clearly shows a faster decline in capacity for the same operating period, indicating that stronger DC-link oscillations translate into higher equivalent cycle numbers and thus accelerated degradation. Conversely, when the ripple factor is reduced, the battery operates under smoother energy trajectories and the remaining capacity stays closer to its initial value, even after long-term operation. This result quantitatively supports the motivation of the proposed energy-aware GFM strategy, which aims at suppressing DC-link energy ripple to alleviate battery cycling stress. Figure 19 compares the evolution of the remaining battery capacity for the conventional fixed-parameter GFM control and the proposed energy-aware GFM strategy. Both curves start from 100% and gradually decline due to the combined effects of calendar aging and cycle aging. However, the proposed control consistently maintains a higher capacity over the entire operating period because the adaptive energy-aware mechanism reduces DC-link energy oscillations and mitigates high-frequency charge–discharge cycling. After 12 years of operation, the conventional method leaves approximately 68.2% remaining capacity, whereas the proposed control preserves about 71.3%, corresponding to a reduction of roughly 4.5% in cumulative degradation. This quantitative comparison demonstrates that, in addition to improving

dynamic stability, the proposed GFM control can effectively extend the usable lifetime of the battery energy storage system.

It should be emphasized that, although multiple enhancements are introduced in the proposed control strategy, their contributions to battery lifetime extension are not equivalent. The dominant factor is the suppression of DC-link energy ripple, which directly reduces high-frequency charge–discharge cycling of the battery. This effect is primarily achieved through the adaptive virtual inductance and energy-aware damping mechanisms, which act on fast electrical dynamics and effectively limit transient power oscillations exchanged between the inverter and the DC-link.

The energy-aware inertia adaptation, while an integral part of the proposed framework, plays a secondary and supervisory role with respect to battery aging. Its primary function is to reshape the frequency–power dynamics under severe disturbances and weak-grid conditions, thereby preventing large energy excursions that could otherwise induce deep or frequent battery cycling. Under nominal operating conditions, where DC-link energy ripple is already well suppressed, the adaptive inertia remains close to its nominal value by design and therefore has limited direct influence on battery lifetime.

In summary, the battery lifetime extension observed in this work mainly originates from fast compensation mechanisms that suppress DC-link energy ripple, whereas the adaptive inertia contributes indirectly by enhancing robustness and preventing operating regimes associated with excessive battery stress. The coordinated action of these mechanisms ensures both short-term dynamic stability and long-term battery durability.

To highlight the improvement in grid-voltage stabilization, additional PCC voltage waveforms and modal analysis results have been included, demonstrating enhanced damping of low-frequency oscillations under weak-grid disturbances. Furthermore, the battery lifetime impact is quantified using the degradation model described in Section 4, showing reduced cycling stress and lower cumulative degradation index under the proposed adaptive GFM control compared with the conventional fixed-parameter approach.

6 Discussion on Sensitivity and Implementation Considerations

Since real-time or hardware-in-the-loop (HIL) validation is not included in this study, it is important to discuss the sensitivity factors and potential implementation risks associated with the proposed multi-timescale energy-aware GFM control strategy.

From a sensitivity perspective, the performance of the proposed controller may be influenced by several practical factors, including DC-link capacitance variation, battery internal resistance uncertainty, and inaccuracies in grid-strength (SCR) estimation. Variations in DC-link capacitance affect the absolute energy level used for inertia and damping scheduling, while battery parameter uncertainty influences the effective energy buffering capability. However, the proposed control relies on low-bandwidth DC-link energy indicators and filtered grid-strength estimates rather than instantaneous measurements, which significantly reduces sensitivity to parameter mismatch and measurement noise. Moreover, the scheduling laws are bounded and rate-limited, ensuring that moderate estimation errors do not lead to abrupt parameter changes or instability.

Regarding implementation risks, practical challenges mainly arise from digital control delays, numerical differentiation used in virtual inductance realization, and saturation effects during large disturbances. These issues are mitigated in the proposed framework through hierarchical timescale separation, where the fast current control operates at the switching timescale, while inertia and virtual inductance adaptation are executed at much slower rates. In addition, low-pass filtering, gain saturation, and smooth mode coordination are explicitly incorporated to prevent discontinuities during mode transitions and large-signal events.

Overall, although experimental or HIL validation is not presented in this manuscript, the controller structure is designed with real-time implementation in mind and is compatible with standard digital control platforms. A comprehensive experimental validation, including sensitivity studies under different load profiles and operating conditions, will be pursued in future work.

7. Conclusion

A cross-timescale energy-aware grid-forming (CTEA-GFM) control strategy for PV–battery systems has been presented. By combining a fast current control with active damping, an adaptive power layer, and a slow supervisory scheduler, the proposed method enhances transient stability while extending battery lifetime. Small-signal

analysis confirmed improved eigenvalue damping under varying operating conditions, and time-domain simulations verified superior DC-link voltage regulation, reduced power oscillations, and seamless GFM–GFL transitions. Compared with conventional control, the proposed strategy offers greater adaptability and resilience, making it well suited for weak-grid integration and emergency power applications.

Author Contributions: Lijun Zheng: Conceptualization, analysis methodology, writing original draft, related technical and material support; Writing- reviewing and editing, Weijie Chen: Writing- reviewing and editing.

Funding : No Funding.

Data availability：All key model parameters used in this study have been provided in the manuscript. Further simulation details are available from the corresponding author upon reasonable request.

References

[1] REN21, Renewables 2023 Global Status Report. Paris, France: REN21 Secretariat, 2023.

[2] International Energy Agency, World Energy Outlook 2023. Paris, France: IEA, 2023.

[3] F. Milano, F. Dörfler, G. Hug, D. J. Hill, and G. Verbič, “Foundations and challenges of low-inertia power systems,” Proc. IEEE, vol. 108, no. 7, pp. 1189–1215, Jul. 2020.

[4] International Renewable Energy Agency, Renewable Capacity Statistics 2023. Abu Dhabi, UAE: IRENA, 2023.

[5] P. Denholm and R. Sioshansi, “The value of energy storage for grid applications,” Proc. IEEE, vol. 109, no. 7, pp. 1131–1152, Jul. 2021.

[6] N. Miller, A. Leonardi, B. H. Chowdhury, and A. Hoke, “Resilient microgrids with PV and storage,” IEEE Power Energy Mag., vol. 19, no. 5, pp. 46–57, Sep.–Oct. 2021.

[7] R. Musca, D. Van Hertem, and G. Denis, “Grid-forming converters: A critical review of pilot projects and demonstrators,” Renew. Sustain. Energy Rev., vol. 162, art. 112449, May 2022.

[8] J. Matevosyan, D. Ramasubramanian, and F. Milano, “Grid-forming inverter-based resource research landscape: Understanding the key assets for renewable-rich power systems,” IEEE Power Energy Mag., vol. 22, no. 2, pp. 56–68, Mar.–Apr. 2024.

[9] H. Wu, X. Wang, F. Blaabjerg, and Y. Yang, “Adaptive fast/slow internal voltage source control of grid-forming converters,” IEEE J. Emerg. Sel. Topics Power Electron., early access, 2023.

[10] Energy Systems Integration Group, Grid-Forming Technology in Energy Systems Integration. Reston, VA, USA: ESIG, 2022.

[11] J. M. Guerrero, P. C. Loh, T. L. Lee, and M. Chandorkar, “Advanced control architectures for intelligent microgrids—Part I: Decentralized and hierarchical control,” IEEE Trans. Ind. Electron., vol. 60, no. 4, pp. 1254–1262, Apr. 2013.

[12] N. Pogaku, M. Prodanovic, and T. C. Green, “Modeling, analysis and testing of autonomous operation of inverter-based microgrids,” IEEE Trans. Power Electron., vol. 22, no. 2, pp. 613–625, Mar. 2007.

[13] Y. Yang, J. Xu, C. Li, W. Zhang, Q. Wu, M. Wen, and F. Blaabjerg, “A new virtual inductance control method for frequency stabilization of grid-forming virtual synchronous generators,” IEEE Trans. Ind. Electron., vol. 70, no. 1, pp. 441–451, Jan. 2023.

[14] M. Lu, S. D. Sudhoff, and R. H. Lasseter, “Controlled inverters with virtual oscillator control,” IEEE Trans. Power Electron., vol. 35, no. 7, pp. 7394–7408, Jul. 2020.

[15] A. D’Arco and M. Liserre, “Virtual synchronous machines: A review,” IEEE Trans. Ind. Electron., vol. 64, no. 7, pp. 4869–4879, Jul. 2017.

[16] M. Chen, D. Zhou, and F. Blaabjerg, “Enhanced transient angle stability control of grid-forming converters based on virtual synchronous generator,” IEEE Trans. Ind. Electron., vol. 69, no. 9, pp. 9133–9144, Sep. 2022.

[17] M. Elmahallawy, T. M. El-Fouly, and A. T. Alouani, “Lithium-ion batteries modeling and state-of-health prediction: A comprehensive review,” IEEE Access, vol. 10, pp. 124035–124069, Nov. 2022.

[18] R. Xiong, J. Tian, W. Shen, and F. Sun, “Lithium-ion battery aging mechanisms and diagnosis for electric vehicle applications,” Renew. Sustain. Energy Rev., vol. 131, art. 110048, Oct. 2020.

[19] T. Rahman, N. Hannan, P. J. Ker, and A. Hussain, “Exploring lithium-ion battery degradation: A concise review,” Batteries, vol. 10, no. 7, art. 220, Jul. 2024.

[20] N. Baeckeland, S. Shah, A. Hoke, J. Johnson, and F. Diaz-Gonzalez, “Overcurrent limiting in grid-forming inverters: A comprehensive review and discussion,” IEEE Trans. Energy Convers., vol. 39, no. 4, pp. 3178–3199, Dec. 2024.